Journal of Hazardous Materials 342 (2018) 69–76

Contents lists available at ScienceDirect

Journal of Hazardous Materials

journal homepage: www.elsevier.com/locate/jhazmat

Research paper

Design of 3D MnO_2/Carbon sphere composite for the catalytic oxidation and adsorption of elemental mercury

Haomiao Xu[a,b], Jinping Jia[a], Yongfu Guo[c], Zan Qu[a], Yong Liao[a], Jiangkun Xie[a], Wenfeng Shangguan[b], Naiqiang Yan[a,*]

[a] School of Environmental Science and Engineering, Shanghai Jiao Tong University, Shanghai, 200240, China
[b] Research Center for Combustion and Environment Technology, School of Mechanical Engineering, Shanghai Jiao Tong University, Shanghai, 200240, China
[c] Suzhou University of Science and Technology, Suzhou, 215009, China

HIGHLIGHTS

- Three-dimensional (3D) MnO_2/Carbon Sphere (MnO_2/CS) composite was synthesized for Hg^0 removal.
- The composite can use the advantages of carbon-based and Mn-based materials.
- The Hg^0 removal efficiency of the composite was higher than α-MnO_2.

GRAPHICAL ABSTRACT

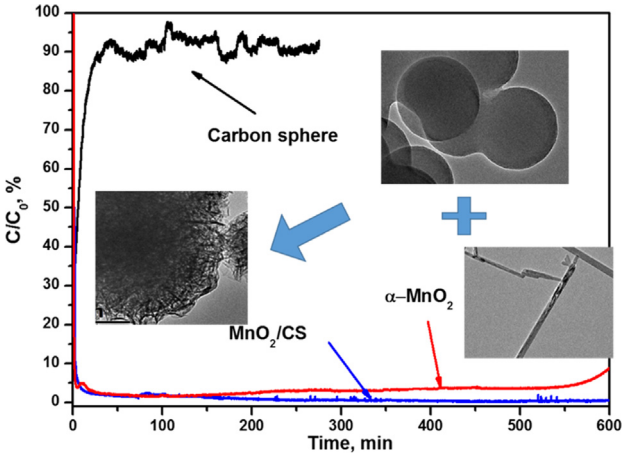

ARTICLE INFO

Article history:
Received 21 April 2017
Received in revised form 3 August 2017
Accepted 6 August 2017
Available online 8 August 2017

Keywords:
Elemental mercury
Carbon sphere
Catalytic oxidation
Hierarchical structure

ABSTRACT

Three-dimensional (3D) MnO_2/Carbon Sphere (MnO_2/CS) composite was synthesized from zero-dimensional carbon spheres and one-dimensional α-MnO_2 using hydrothermal method. The hierarchical MnO_2/CS composite was applied for the catalytic oxidation and adsorption of elemental mercury (Hg^0) from coal-fired flue gas. The characterization results indicated that this composite exhibits a 3D urchin morphology. Carbon spheres act as the core and α-MnO_2 nano-rods grew on the surface of carbon spheres. This 3D hierarchical structure benefits the enlargement of surface areas and pore volumes. Hg^0 removal experimental results indicated that the MnO_2/CS composite has an outstanding Hg^0 removal performance due to the higher catalytic oxidation and adsorption performance. MnO_2/CS composite had higher than 99% Hg^0 removal efficiency even after 600 min reaction. In addition, the nano-sized MnO_2/CS composite exhibited better SO_2 resistance than pure α-MnO_2. Moreover, the Hg-TPD results indicated that the adsorbed mercury can release from the surface of MnO_2/CS using a thermal decomposition method.

© 2017 Elsevier B.V. All rights reserved.

* Corresponding author at: School of Environmental Science and Engineering, Shanghai Jiao Tong University, Shanghai, 200240, China.
E-mail address: nqyan@sjtu.edu.cn (N. Yan).

http://dx.doi.org/10.1016/j.jhazmat.2017.08.011
0304-3894/© 2017 Elsevier B.V. All rights reserved.

1. Introduction

Mercury was hazardous element in the environment [1]. The emission of mercury from human activities results in a high level of mercury background value of atmosphere. Generally, coal-fired power plant was regard as the largest one among various emission sources, such as cement plant, non-ferrous smelting plant, waste incineration plant, etc [2,3]. Controlling the emission from coal-fired power plant was significant for mercury control. In addition, mercury exists as the state of elemental mercury (Hg^0) was hard to be removed due to its insolubility and high volatility. Among various studies, adsorption and catalytic oxidation were two primary mechanisms for the control of Hg^0 [4–7]. Adsorption technology can capture the oxidized mercury (Hg^{2+}), particle-bond mercury (Hg^p) and Hg^0 in the flue gas. Catalytic oxidation method can make insoluble Hg^0 oxidize to Hg^{2+}. Then the soluble Hg^{2+} can be removed in wet flue gas desulfurization system [8]. However, mercury enriched in the slurry could cause mercury secondary contamination. Therefore, adsorption technology seems as a potential method for Hg^0 control.

A promising sorbent was the key when using adsorption technology [6,7,9]. Based on previous studies, the efficient Hg^0 sorbent can be classified into two primary types: carbon based materials and transition metal oxides [4,9,10]. Active carbon which has high surface areas and functional groups, were beneficial for Hg^0 adsorption. However, it was limited for a wide usage due to its low Hg^0 efficiency and high cost. In addition, the spent carbon could decrease the quality of fly ashes [11]. Cl^- or Br^- modified active carbons were selected to enhance the Hg^0 removal performance [6,12]. However, the cost was further increased. Recently, transition metal oxides such as FeO_x, MnO_x and CuO_x were developed for Hg^0 removal [4,13]. Among these metal oxides, Mn-based oxides are generally considered as the most promising materials due to the low cost, environmental friendliness and natural abundance [14]. They have been indicated to have high Hg^0 adsorption capacity due to the chemical-adsorption of mercury on its surface. Higher valance state of Mn, larger surface areas and sufficient surface oxygen are beneficial for Hg^0 removal based on previous studies [15–18]. However, manganese oxides often suffer from the low electron transfer performance, small surface area and SO_2 poisoning [13].

To solve the defects of Mn-based oxides, modifications of Mn-based oxides were widely investigated. Carbon supported Mn-based oxides can enlarge the surface area and enhance the adsorption performance [19–22]. In our recent studies, emerging graphene was used as a material support for MnO_x [16] Graphene enhanced the electrical conductivity of MnO_x, and highly dispersed MnO_x particles could be readily deposited on graphene nanosheets. Carbon based materials can solve the problems of poor electrical conductivity and small surface area. However, the two-dimensional graphene sheets cover the Mn active sites, resulted in low activities to some extent. Designing a better structure of the carbon based materials and Mn-based oxides can make full use of their advantages. A three-dimensional (3D) structure benefits for gas diffusion and chemical reaction [23,24]. Core-shell structured 3D nanocomposites have a rapidly growing owing to combination of the respective properties of cores and shells [25,26]. Carbon sphere was one of carbon materials for the cores due to its chemically modification surface [27,28]. It exhibited a zero-dimensional (0D) structure and acted as the core of composite. In addition, it has the properties of carbon-based materials such as electron transitions and sufficient surface functional oxygen groups. These functional groups were favorable for Mn-based materials in-situ grew on its surface. Among various Mn-based materials, α-MnO_2 had super performance than other crystal form of MnO_2 [15]. The one-dimensional (1D) α-MnO_2 acted as the shell could build the 3D structure of MnO_2/Carbon sphere (MnO_2/CS) composite. Until now, there are no reports using 1D α-MnO_2 and 0D carbon sphere to synthesize a 3D MnO_2/CS composite.

Herein, in this study, 3D MnO_2/CS composite was synthesized using simple hydrothermal method. The composite was characterized using FT-IR, XPS, Raman, XRD and TEM analysis. The Hg^0 removal performance was evaluated in a fixed-bed adsorption system. Moreover, the effects of O_2, SO_2 and the Hg^0 removal mechanism were also investigated.

2. Experimental section

2.1. Synthesis of MnO_2/CS 3D material

Carbon sphere support was synthesized using a hydrothermal method. Glucose was chosen as the carbon souse. Generally, 5.0 g glucose was dissolved in 100 mL ultrapure water and then transfer into a 150 mL Teflon hydrothermal synthesized reactor, kept 200 °C for the reaction of 10 h. After that, the product was washed for three times with ultrapure water and kept warming at 105 °C for 12 h. The carbon sphere was synthesized. MnO_2/CS was also synthesized using a hydrothermal method. 1.0 g of the above carbon sphere was dissolve in ultrapure water under ultrasonic dispersion for 30 min. After that, 5 mmol $MnSO_4{\cdot}H_2O$ were added and keep stirring for 180 min. Then 5 mmol $KMnO_4$ were slowly added in the above solution and kept stirring for 60 min. The above mixture then transferred into a Telfon-lined autoclave. The autoclave temperature was maintained at 160 °C for 12 h, and the obtained precipitates were washed with water and dried at 80 °C for 12 h. For compassion, α-MnO_2 was prepared according to same method without carbon sphere.

2.2. Characterization

Power X-ray diffraction (XRD) patterns were recorded on a X-ray diffractometer (APLX-DUO, BRUKER, Germany) with Cu Kα radiation. The data were collected in the 2θ range 10° to 80° with a scanning velocity of 10°/min. Nitrogen sorption isotherms were measured at −196 °C using a quartz tube (Quantachrome 2200e). Before measurements, the samples were degassed in a vacuum at 200 °C for 5 h. The Brunauer-Emmett-Teller (BET) method was utilized to calculated the specific surface areas using multi adsorption and desorption data. The Barrett-Joyner-Halenda (BJH) pore volumes and pore size were also calculated. Raman scattering spectra were performed on a SENTERRA R200. FTIR spectroscopy was carried out to characterize the surface properties. The micrographs were obtained in the bright-field imaging mode at an acceleration voltage of 120 kV. The 633 nm line of Ar^+ laser was used for the excitation. Transmission electronic microscopy (TEM) images were taken with a JEOLJEM-2010 operated at 200 kV. The H_2-TPR experiments were performed on a Chemisorp TPx 290 instrument; the samples were degassed at 200 °C for 3 h under Ar atmosphere before the tests, and the reducing gas was 10% H2/Ar. X-ray photoelectron spectroscopy (XPS) results were recorded with an Ultra DLD (Shimadzu–Kratos) spectrometer with Al Kα as the excitation source, and the C 1 s line at 284.6 eV was used as a reference for the binding energy calibration.

2.3. Hg^0 removal test

A lab-scale fixed-bed adsorption system was assembled, as shown in Supporting Information (Fig. S1), to explore the Hg^0 removal efficiencies by the as-prepared materials. The fixed-bed reactor was constructed to allow for a total gas flow of 500 mL/min at temperatures from 100 to 300 °C. Thirty milligrams of a sorbent was used for each experiment and it was put in a quartz tube with

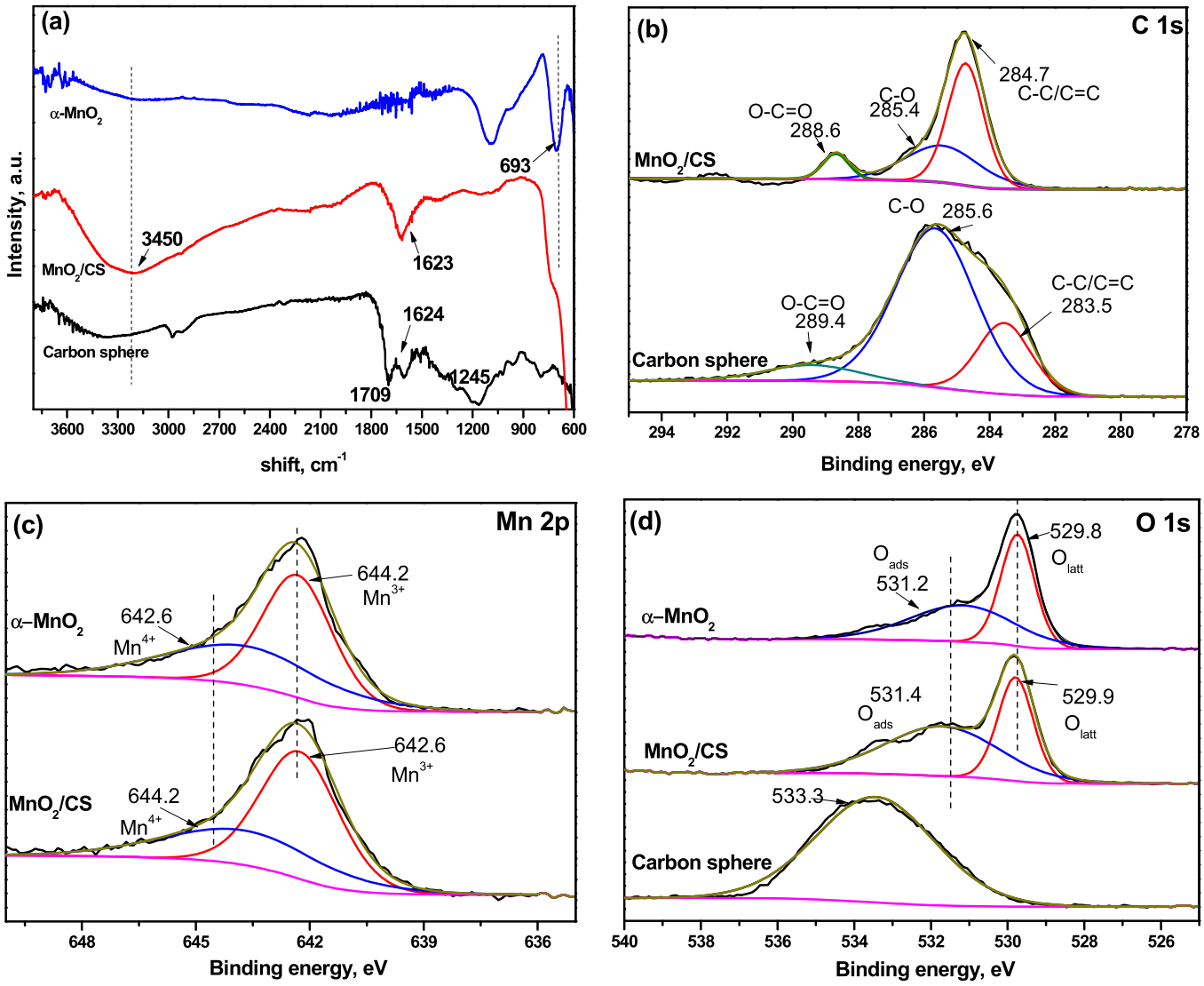

Fig. 1. (a) FT-IR spectra of as-prepared samples, (b) C 1s, (c) Mn 2p and (d) O 1 s spectra of XPS analysis for the as-prepared samples.

a diameter of 4 cm. During the test, the mercury inlet gas bypassed the sorbent and passed into the analytical system until the desired inlet mercury concentration was established. A cold vapor atomic absorption spectrometer mercury detector (CVASS) was used for detection the concentration of off-gas, which was calibrated by Lumex RA 915+. Temperature control devices were installed to control the mixed gas and the reactor temperature. The tests were carried out in the reactor that was maintained at 100–300 °C under Hg^0-laden nitrogen flow. In addition, active carbon was used for the off-gas cleaning. It can adsorb the mercury (Hg^{2+} and Hg^0) in the flue gas. $H_2SO_4 + KMnO_4$ solution was used for adsorbed the oxidized mercury. To investigate the effect of temperature on the flue gas, the area under the breakthrough curves corresponding to Hg^0 on the prepared sorbents during 600 min was integrated. To investigate the effects of various gas components, pure N_2, 4% O_2 and 500 ppm of SO_2 were chosen when needed. The Hg^0 removal efficiency was calculated according to Eq. (1):

$$Removal\quad efficiency = \frac{Hg^0_{in} - Hg^0_{out}}{Hg^0_{in}} \tag{1}$$

where the $Hg_{in}{}^0$ is the inlet concentration of Hg^0, and $Hg_{out}{}^0$ is the outlet concentration of Hg^0.

Mercury-temperature programmed desorption (Hg-TPD) method was designed to investigate the mercury release performance from the spent material. After mercury adsorption at 150 °C with 4% O_2 for 30 min, the sorbents were regenerated by heating from 100 °C to 700 °C in a pure N_2 carrier gas. Hg-TPD curves under different heating rates (2 °C/min, 5 °C/min and 10 °C/min) on the MnO_2/CS surfaces were collected.

3. Results & discussion

3.1. Physical and chemical characterization

FT-IR spectra were recorded to investigate the surface chemical compositions of the prepared samples. Fig. 1(a) shows the spectra of carbon spheres, α-MnO_2 and MnO_2/CS. For carbon spheres, peaks appeared at 1709, 1624 and 1245 were cm^{-1} the C=O, the aromatic C=C and the epoxy C—O, respectively [16,29]. A wide peak at ~3450 cm^{-1} was the O—H of the adsorbed water molecules [16]. For α-MnO_2, the peaks at 693 cm^{-1} was the Mn-O vibrations of [MnO_6] octahedra in α-MnO_2 [30]. After hydrothermal reactions, in the case of MnO_2/CS, the functional peaks of C=O and C—O disappeared according to its spectrum. The peak at 1623 cm^{-1} which was ascribed to C=C bond still existed. In addition, the vibration of

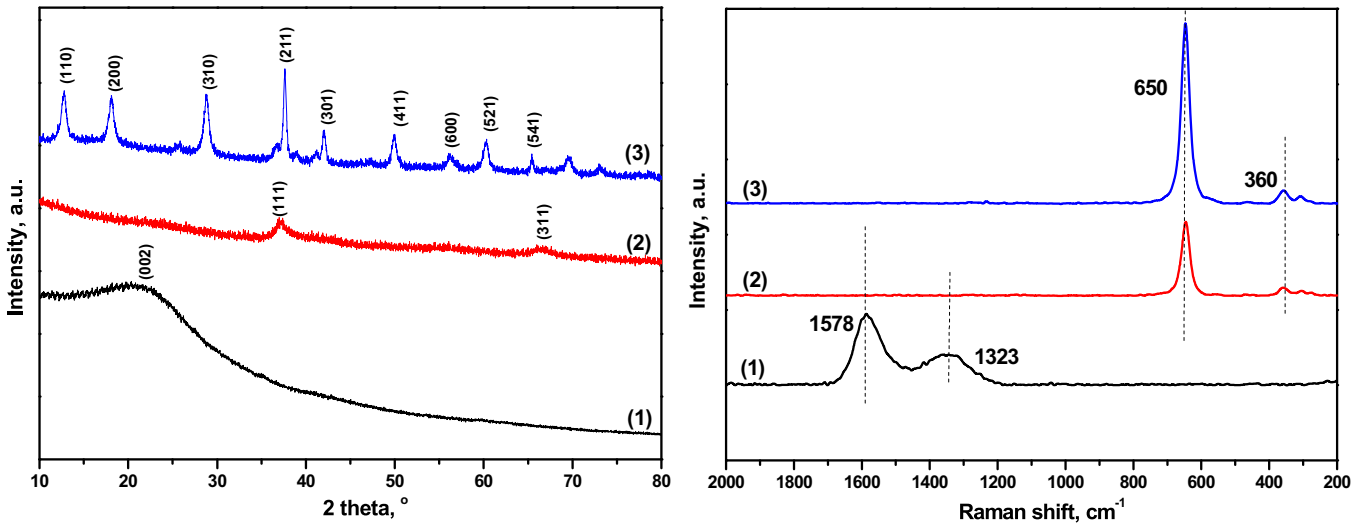

Fig. 2. (a) XRD patterns and (b) Raman spectra of (1) carbon spheres, (2) MnO_2/CS, and (3) α-MnO_2.

Mn-O below 700 cm^{-1} can be detected. The results indicated that manganese oxides grow on the surface of carbon sphere, combing with the surface chemical function groups.

XPS analysis of as-prepared samples were presented in Fig. 1 (b), (c) and (d). As shown in Fig. 1(b), the XPS spectra of C 1 s are given, for carbon sphere, the peaks at 283.5, 285.6 and 289.4 eV were corresponded to C—C/C=C groups in aromatic rings, C—O groups (epoxy and alkoxy), and O—C=O groups, respectively [16]. The ratio of C—O/C was high (70.68%), indicated that lots of C—O functional groups on the surface of carbon sphere and the result was meet with the FT-IR analysis. For MnO_2/CS composite, three peaks at 284.7, 285.4 and 288.6 eV can be assigned to C—C/C=C, C—O and O—C=O groups, respectively. It was obvious that there is a sharp decrease in the ratio of C—O/C (decreased to 35.23%), indicated that C—O function groups were the primary binding sites in the synthesized process. In the spectra of Mn 2p3/2, as shown in Fig. 1(c), for α-MnO_2, two peaks could be divided into two components at 642.6 and 644.2 eV corresponded to Mn^{3+} and Mn^{4+}, respectively [14,31,32]. The high binding energy is ascribed to high valance of Mn. Generally, higher valance of Mn is favorable for catalytic oxidation. The same peaks were detected in the spectra of MnO_2/CS composite. However, the ratio of $Mn^{4+}/Mn^{3+}+Mn^{4+}$ (36.03%) was a little decreased to that of α-MnO_2, due to the reduction effect of C. For the spectrum of O 1s, as shown in Fig. 1(d), a wide peak of carbon sphere centered at 533.3 eV. The peaks at binding energies higher than 533 eV were associated with adsorbed water. There were two peaks at 529.8 and 531.2 eV corresponded to lattice oxygen (O_{latt}) and adsorbed oxygen (O_{ads}), respectively [15,33]. For MnO_2/CS composite, two peaks at 529.9 and 531.4 eV were also corresponded to O_{latt} and O_{ads}, respectively. However, the ratio of $O_{ads}/O_{latt}+O_{ads}$ increased from 50.32 to 60.87% due to the sufficient surface oxygen of carbon sphere. Higher surface oxygen on the composite surface was beneficial for catalytic reactions.

The crystal structures of the as-prepared materials were characterized by XRD analysis. As shown in Fig. 2(a), it gives the patterns of carbon spheres, MnO_2/CS and α-MnO_2. For carbon sphere, a wide peak was detected at ~25°, corresponding to the (002) diffraction peak of carbon. For α-MnO_2, the character peaks were well corresponded to pure α-MnO_2(JCPDS 44-0141) [15,34]. With the addition of 10 mmol MnO_2 on 1 g of carbon spheres, two peaks at

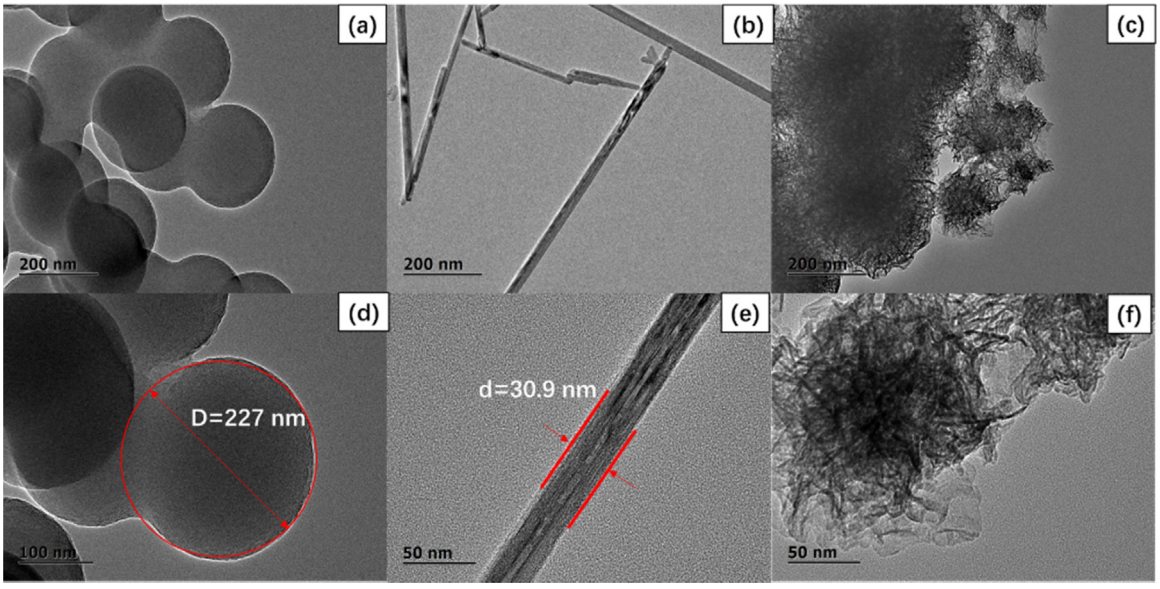

Fig. 3. TEM images of carbon sphere ((a) and (d)), α-MnO_2 ((b) and (e)) and MnO_2/CS composite ((c) and (f)).

36.9°and 66.5° were correspond to the phase of (111) and (311) for birnessite-type MnO_2, respectively. For the pattern of MnO_2/C composite, two peaks at 36.8°and 65.7 °correspond to the (111) and (311) phases birnessite-type MnO_2, respectively [28].

To further investigate the textural properties of these materials, Raman spectra are given and shown in Fig. 2(b). For carbon sphere, the peaks at 1323 and 1578 cm^{-1} were corresponded to the D bond and G bond, respectively. In which, the G bond represented the in-plane vibration of graphite crystals and that the D bond was the vibration of amorphous carbon. The ratio of peak values (I_D/I_G) was smaller than 1, indicated that the surface defect existed on carbon sphere. For α-MnO_2, in the low wave number regions, two weak bands at 650 and 360 cm^{-1} can also be observed [35]. They were corresponded to the symmetric stretching vibration M-O of [MnO_6] groups and Mn-O stretching vibration in the basal plane of [MnO_6] sheet [25]. With the addition of 10 mmol MnO_2, there were also two peaks at 650 and 360 cm^{-1} can be detected. However, the intensity was not as strong as pure α-MnO_2. There were no peaks for the spectrum of carbon sphere, indicated that manganese oxides mainly existed on the surface of MnO_2/CS composite.

Fig. 3 shows the TEM images of carbon sphere, α-MnO_2 and MnO_2/CS composite. It was seen that all carbon spheres were uniform in size with an average diameter of ~227 nm. The carbon spheres were linked with each other due to the hydrothermal conditions. For α-MnO_2, they exhibited one-dimensional nano-rods, which had the diameter of about 30.9 nm. For MnO_2/CS composite, it exhibited a 3D structure. As shown in Fig. 3(c), MnO_2/CS composite exhibited as the urchin morphology where the carbon sphere was the core of 3D material, and the MnO_2 nano-rods grow on the surface of carbon spheres. The sufficient function groups on the surface of carbon sphere support for Mn ions. The nano-rod like MnO_2 can grow on its surface (detail images can also see in Fig. S2). Such hierarchical structure of this 3D material was beneficial for enlarging the surface areas.

As shown in Table 1, the BET surface areas, the BJH pore volumes and average pore sizes were given. Carbon sphere has the surface areas of only 8.628 m^2/g due to its large sphere and low pore volume (ca. 0.010 m^3/g). The one dimensional α-MnO_2 had the surface area of 31.013 m^2/g. The pore volume and the pore dimeter were 0.066 cm^3/g and 3.693 nm. After 3D structure formation, the surface of MnO_2/CS was four times larger than α-MnO_2, which was 134.095 m^2/g. In addition, the pore volume of MnO_2/CS (ca. 0.331 m^3/g) was five times larger than that of α-MnO_2. The pore dimeter was similar to that of α-MnO_2. With the designing of 3D structure MnO_2/CS, the surface areas and pore volume were significantly enlarged.

3.2. Hg^0 removal performance

As shown in Fig. 4(a), Hg^0 removal performances of these as-prepared materials were tested. Obviously, pure carbon sphere had no activity for Hg^0. α-MnO_2 was evaluated for Hg^0 removal and it exhibited a high Hg^0 removal efficiency. But it is lower than that of MnO_2/CS composite. MnO_2/CS composite had excellent Hg^0 removal performance. The Hg^0 removal efficiency could keep approximately 100% even after 600 min reaction. In addition, the effect of temperature on Hg^0 removal efficiencies were tested and the results are shown in Fig. 4(b). Carbon sphere, α-MnO_2 and 10 mmol MnO_2/CS were evaluated at a temperature window of 100–350 °C. The Hg^0 removal efficiencies were calculated based on the total 600 min reaction. Carbon sphere also had nearly no removal efficiency at such a wide temperature window. For α-MnO_2, the highest Hg^0 removal efficiency was at 150 °C and it was 91.73%. With the temperature rising, the Hg^0 removal efficiencies dropped sharply. The efficiencies were 64.8% at 250 °C and 28% at 350 °C, respectively. For MnO_2/CS, the Hg^0 removal efficiency was

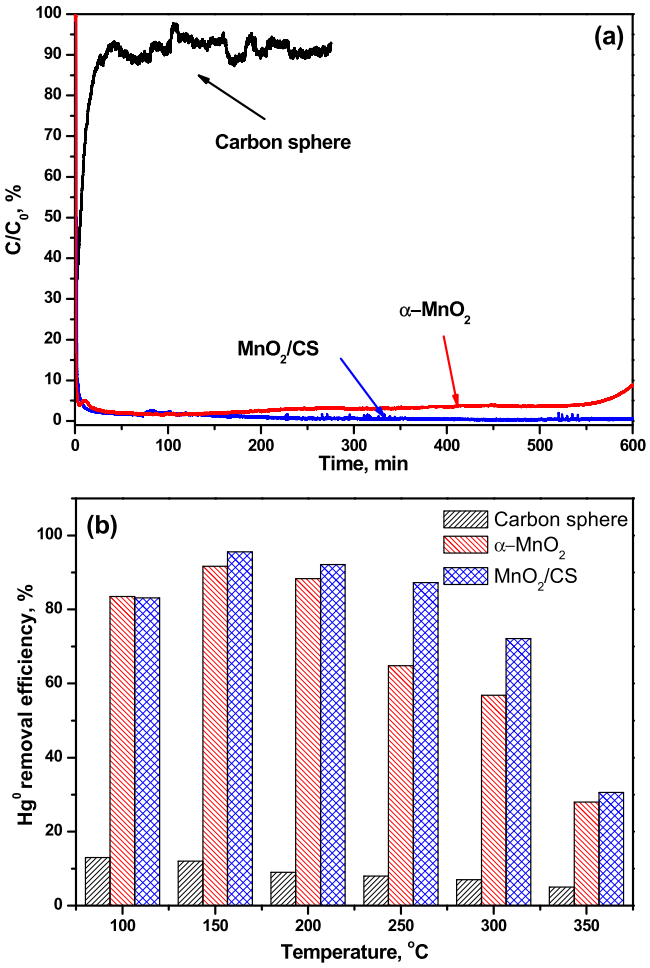

Fig. 4. (a) Hg^0 removal performance of as-prepared samples and (b) the total 600 min Hg^0 removal efficiencies at a wide temperature window.

almost the same to α-MnO_2 at 100 °C. The highest Hg^0 removal efficiency was at 150 °C and it was 95.6%. However, temperature rising did not result in Hg^0 removal efficiency as low as α-MnO_2. Even at 300 °C, it had 72.16% Hg^0 removal efficiency, compared to 56.85% for α-MnO_2. But at 350 °C, the efficiency dropped to 30.6%. Such high temperature was not favorable for Hg^0 removal over Mn-based oxides. Based on the above results, it was indicated that the CS support can enhance the Hg^0 removal efficiency and enlarge the reaction temperature window.

Furthermore, the effects of gas components on Hg^0 removal were investigated. The results of the effects of O_2 and SO_2 are shown in Fig. 5. For α-MnO_2, when there was no O_2 in the simulated flue gas, it had ~95% Hg^0 removal efficiency in the initial 100 min. However, the Hg^0 removal efficiency gradually lost. After 600 min reaction, it almost had no activity for Hg^0 removal. It indicated that O_2 played an important role in Hg^0 removal process. When the gas component was 4% O_2 + 500 ppm SO_2, α-MnO_2 was poisoned for Hg^0 removal. Hg^0 removal efficiency was only ~80% in the initial several minutes, and the Hg^0 removal efficiency gradually decreased. Mn-based oxides can be easily poisoned by SO_2, resulting in low reaction activity. For MnO_2/CS composite, when there was no O_2 in the simulated gas, the Hg^0 removal efficiency was higher than 95% even after 600 min reaction. Sufficient surface oxygen make the material have high Hg^0 removal efficiency. SO_2 had a poison effect on Hg^0 removal over MnO_2/CS. But its poison impact was not as harmful as α-MnO_2. The Hg^0 removal efficiency was approximately 70% after 600 min reaction with 4% O_2 + 500 ppm

Table 1
Surface analysis of as-prepared samples.

Material	BET surface area (m^2/g)	Pore volume (m^3/g)	Pore diameter (nm)	$Mn^{4+}/Mn^{4+}+Mn^{3+}$ (%)	$O_{ads}/O_{ads}+O_{latt}$ (%)	C-O/Total C (%)
Carbon sphere	8.628	0.010	3.352	/	/	70.68
α-MnO_2	31.013	0.066	3.693	42.35	50.32	/
MnO_2/CS	134.095	0.331	3.646	36.03	60.87	35.23

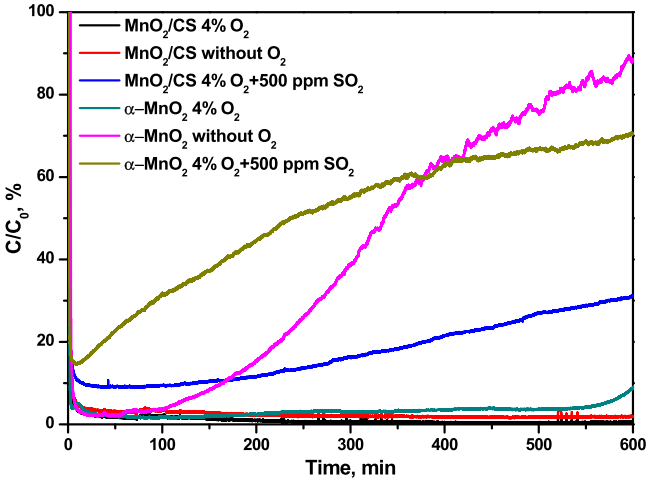

Fig. 5. Effects of O_2 and SO_2 on Hg^0 removal over α-MnO_2 and 3D MnO_2/CS composite.

SO_2. The nano-size 3D material could make full use of the active sites and protect the poison from SO_2. The reason for the poison was that sufficient surface oxygen can combine with the oxidized SO_2 to generate sulfate on its surface. However, carbon-based material has little effect on SO_2 poison due to the porous structure. Sulfate species can not easily generate on its surface.

3.3. Hg^0 removal mechanism over MnO_2/CS

As shown in Fig. 6, the H_2-TPR profile was given to illustrate the reducibility of α-MnO_2 and MnO_2/CS composite. For α-MnO_2, a reduction peak was centered at 331.1 °C which was assigned to the reduction of $Mn^{4+} \rightarrow Mn^{3+} \rightarrow Mn^{2+}$. However, for the profile of MnO_2/CS composite, two reduction peaks can be detected. One peak at 264.6 °C was the reduction peak of $Mn^{4+} \rightarrow Mn^{3+}$, and another peak at 449.4 °C was the peak of $Mn^{3+} \rightarrow Mn^{2+}$. The reduction peak of $Mn^{4+} \rightarrow Mn^{3+}$ shifted to the lower temperature which was beneficial for Hg^0 catalytic oxidation. The mainly active valance of Mn was the higher valance Mn (Mn^{4+}) based on previous studies.

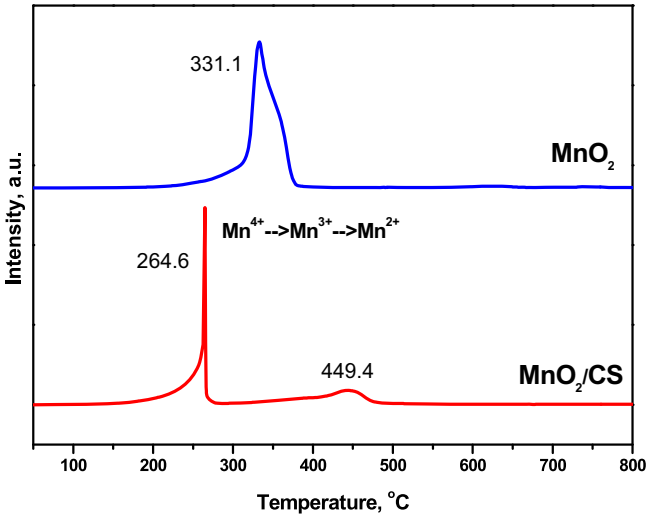

Fig. 6. H_2-TPR profile of α-MnO_2 and MnO_2/CS composite.

In addition, Hg-TPD profile was tested to explore the mercury desorption performance. The results of the Hg-TPD curves under different heating rates are shown in Fig. 7. As shown in Fig. 7(a), under the heating rate of 2 °C/min, two desorption peaks can be detected. One low temperature peak was at 193.2 °C and another high temperature peak was at 400.3 °C. The adsorbed Hg^0 can be absolutely desorbed from the surface of MnO_2/CS, indicated that mercury was adsorbed on the surface of MnO_2/CS. The low temperature peak was ascribed to the physical adsorption and the high temperature peak was due to the chemical adsorption of mercury.

Based on above analysis, the Hg^0 removal mechanism over MnO_2/CS can be described as follows:

$$Hg^0(g) \rightarrow Hg^0(ads) \quad (2)$$

$$Hg^0(ads) + Mn^{4+} \rightarrow Hg^{2+}(ads) + Mn^{3+} \quad (3)$$

$$Hg^{2+}(ads) + O(sur) \rightarrow HgO(ads) \quad (4)$$

It was obvious that Hg^0 removal mechanism was ascribed to a chemical-adsorption process. The high valance of Mn, the electron transition through carbon-based materials, and sufficient was favorable for mercury oxidation. Moreover, such 3D composite which combines porous structure, larger surface area and sufficient binding site, benefits gas adsorption and results in high Hg^0 removal efficiency.

In addition, the desorption under the heating rates of 5 and 10 °C/min were illustrated in Fig. 7(b) and (c). Obviously, two desorption peaks can be detected. The higher heating rates could result in a higher desorption temperature peak. Based on the desorption data under different rates of heating, the desorption activation energy was calculated according to Eq. (5) [16]:

$$2LnT_p - Ln\beta = \frac{E_d}{RT_p} + Ln\frac{E_d}{AR} \quad (5)$$

where T_p is the maximum value at a certain temperature (K), β is the heating rate (K/min), Ed is the desorption activation energy (kJ/mol), R is the gas constant, T is the temperature (K), and A is a pre-exponential factor.

According to the equation, the desorption activation energies of low temperature peak and high temperature peak were 25.38 kJ/mol and 123.05 kJ/mol, respectively.

4. Conclusions

In summary, the MnO_2/CS composite was synthesized using hydrothermal method. The 0D carbon sphere and 1D α-MnO_2 build the 3D urchin-like morphology. The surface area was enlarged along with the enlargement of pore volume. Carbon spheres provide sufficient function groups for Mn ions. The 1D MnO_2 grow on carbon spheres and form the 3D hierarchical structure. The MnO_2/CS composite exhibited higher Hg^0 removal performance than α-MnO_2. Noteworthy, it reveals the SO_2 resistance when used as Hg^0 sorbent. The Hg^0 removal mechanism was mainly ascribed to a chemical-adsorption process. Higher valance of Mn oxidized Hg^0 to oxidized mercury, along with the adsorption with surface oxygen. The larger BET surface areas, abundant surface oxygen and

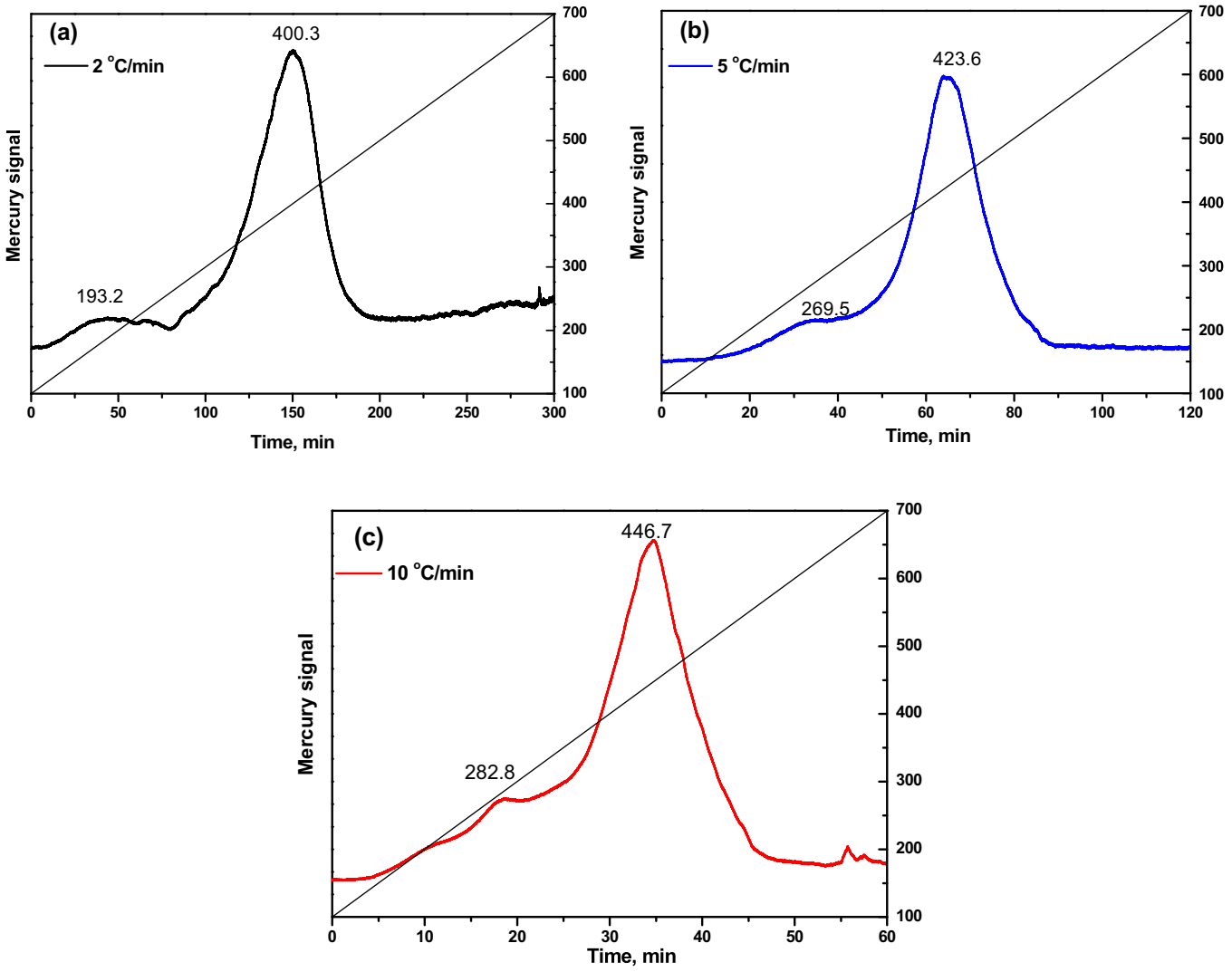

Fig. 7. Hg-TPD profile of MnO_2/CS composite under different heating rates: (a) 2 °/min, (b) 5 °/min, and (c) 10 °/min.

strong reducibility were favorable for Hg^0 oxidation and adsorption. Design of this 3D structure composite by the cooperation of 0D carbon sphere and 1D MnO_2 was promising material for gas purification.

Acknowledgements

This study was supported by National Key R&D Program of China (2017YFC0210502), the Major State Basic Research Development Program of China (973 Program, No. 2013CB430005), and the National Natural Science Foundation of China (No. 51478261, No. 21677096). Thanks for the Natural Science Foundation of Jiangsu Province (BK 20141179) and postdoctoral innovative talent plans (No. BX201700151).

Appendix A. Supplementary data

Supplementary data associated with this article can be found, in the online version, at http://dx.doi.org/10.1016/j.jhazmat.2017.08.011.

Reference:

[1] W.C. Li, H. Tse, Health risk and significance of mercury in the environment, Environ. Sci. Pollut. Res. 22 (2015) 192–201.
[2] E.G. Pacyna, J. Pacyna, K. Sundseth, J. Munthe, K. Kindbom, S. Wilson, F. Steenhuisen, P. Maxson, Global emission of mercury to the atmosphere from anthropogenic sources in 2005 and projections to 2020, Atmos. Environ. 44 (2010) 2487–2499.
[3] L. Zhang, S. Wang, L. Wang, Y. Wu, L. Duan, Q. Wu, F. Wang, M. Yang, H. Yang, J. Hao, Updated emission inventories for speciated atmospheric mercury from anthropogenic sources in China, Environ. Sci. Technol. 49 (2015) 3185–3194.
[4] Y. Gao, Z. Zhang, J. Wu, L. Duan, A. Umar, L. Sun, Z. Guo, Q. Wang, A critical review on the heterogeneous catalytic oxidation of elemental mercury in flue gases, Environ. sci. Technol. 47 (2013) 10813–10823.
[5] Y. Zheng, A.D. Jensen, C. Windelin, F. Jensen, Review of technologies for mercury removal from flue gas from cement production processes, Prog. Energy Combust. Sci. 38 (2012) 599–629.
[6] J.H. Pavlish, E.A. Sondreal, M.D. Mann, E.S. Olson, K.C. Galbreath, D.L. Laudal, S.A. Benson, Status review of mercury control options for coal-fired power plants, Fuel Process. Technol. 82 (2003) 89–165.
[7] J.H. Pavlish, L.L. Hamre, Y. Zhuang, Mercury control technologies for coal combustion and gasification systems, Fuel 89 (2010) 838–847.
[8] M. Dĺaz-Somoano, S. Unterberger, K.R. Hein, Mercury emission control in coal-fired plants: the role of wet scrubbers, Fuel Process. Technol. 88 (2007) 259–263.
[9] S. Sjostrom, M. Durham, C.J. Bustard, C. Martin, Activated carbon injection for mercury control: overview, Fuel 89 (2010) 1320–1322.
[10] Z. Tan, L. Sun, J. Xiang, H. Zeng, Z. Liu, S. Hu, J. Qiu, Gas-phase elemental mercury removal by novel carbon-based sorbents, Carbon 50 (2012) 362–371.

[11] C.L. Senior, S.A. Johnson, Impact of carbon-in-ash on mercury removal across particulate control devices in coal-fired power plants, Energy Fuels 19 (2005) 859–863.
[12] S.B. Ghorishi, R.M. Keeney, S.D. Serre, B.K. Gullett, W.S. Jozewicz, Development of a Cl-impregnated activated carbon for entrained-flow capture of elemental mercury, Environ. sci. Technol. 36 (2002) 4454–4459.
[13] H. Xu, J. Xie, Y. Ma, Z. Qu, S. Zhao, W. Chen, W. Huang, N. Yan, The cooperation of Fe Sn in a MnOx complex sorbent used for capturing elemental mercury, Fuel 140 (2015) 803–809.
[14] C. He, B. Shen, J. Chen, J. Cai, Adsorption and oxidation of elemental mercury over Ce-MnO x/Ti-PILCs, Environ. sci. Technol. 48 (2014) 7891–7898.
[15] H. Xu, Z. Qu, S. Zhao, J. Mei, F. Quan, N. Yan, Different crystal-forms of one-dimensional MnO 2 nanomaterials for the catalytic oxidation and adsorption of elemental mercury, J. Hazard. Mater. 299 (2015) 86–93.
[16] H. Xu, Z. Qu, C. Zong, W. Huang, F. Quan, N. Yan, MnO x/Graphene for the catalytic oxidation and adsorption of elemental mercury, Environ. sci. Technol. 49 (2015) 6823–6830.
[17] H. Xu, Z. Qu, C. Zong, F. Quan, J. Mei, N. Yan, Catalytic oxidation and adsorption of Hg 0 over low-temperature NH 3-SCR LaMnO 3 perovskite oxide from flue gas, Appl. Catal. B: Environ. 186 (2016) 30–40.
[18] J. Li, N. Yan, Z. Qu, S. Qiao, S. Yang, Y. Guo, P. Liu, J. Jia, Catalytic oxidation of elemental mercury over the modified catalyst Mn/α-Al2O3 at lower temperatures, Environ. Sci. Technol. 44 (2017) 426–431.
[19] L. Wang, B. Huang, Y. Su, G. Zhou, K. Wang, H. Luo, D. Ye, Manganese oxides supported on multi-walled carbon nanotubes for selective catalytic reduction of NO with NH 3: Catalytic activity and characterization, Chem. Eng. J. 192 (2012) 232–241.
[20] Y. Gorlin, C.-J. Chung, D. Nordlund, B.M. Clemens, T.F. Jaramillo, Mn3O4 supported on glassy carbon: an active non-precious metal catalyst for the oxygen reduction reaction, ACS Catal. 2 (2012) 2687–2694.
[21] M. Sui, S. Xing, L. Sheng, S. Huang, H. Guo, Heterogeneous catalytic ozonation of ciprofloxacin in water with carbon nanotube supported manganese oxides as catalyst, J. Hazard. Mater. 227 (2012) 227–236.
[22] Y. Wang, C. Ge, L. Zhan, C. Li, W. Qiao, L. Ling, MnO x–CeO2/Activated carbon honeycomb catalyst for selective catalytic reduction of NO with NH3 at low temperatures, Ind. Eng. Chem. Res. 51 (2012) 11667–11673.
[23] L. Zhang, L. Shi, L. Huang, J. Zhang, R. Gao, D. Zhang, Rational design of high-Performance DeNO x catalysts based on Mn x co3?x O4 nanocages derived from Metal?Organic frameworks, ACS Catal. 4 (2014) 1753–1763.
[24] Z. Sun, Q. Yue, Y. Liu, J. Wei, B. Li, S. Kaliaguine, Y. Deng, Z. Wu, D. Zhao, Rational synthesis of superparamagnetic core–shell structured mesoporous microspheres with large pore sizes, J. Mater. Chem. A 2 (2014) 18322–18328.
[25] Z. Lei, J. Zhang, X. Zhao, Ultrathin MnO2 nanofibers grown on graphitic carbon spheres as high-performance asymmetric supercapacitor electrodes, J. Mater. Chem. 22 (2012) 153–160.
[26] X. Lu, M. Yu, G. Wang, T. Zhai, S. Xie, Y. Ling, Y. Tong, Y. Li, H-TiO2@ MnO2//H-TiO2@ C Core–Shell nanowires for high performance and flexible asymmetric supercapacitors, Adv. Mater. 25 (2013) 267–272.
[27] W. Xiao, J.S. Chen, Q. Lu, X.W. Lou, Porous spheres assembled from polythiophene (PTh)-coated ultrathin MnO2 nanosheets with enhanced lithium storage capabilities, J. Phys. Chem. C 114 (2010) 12048–12051.
[28] G. Wang, H. Xu, L. Lu, H. Zhao, One-step synthesis of mesoporous MnO 2/carbon sphere composites for asymmetric electrochemical capacitors, J. Mater. Chem. A 3 (2015) 1127–1132.
[29] F. Ma, H. Zhao, L. Sun, Q. Li, L. Huo, T. Xia, S. Gao, G. Pang, Z. Shi, S. Feng, A facile route for nitrogen-doped hollow graphitic carbon spheres with superior performance in supercapacitors, J. Mater. Chem. 22 (2012) 13464–13468.
[30] H. Wang, Z. Lu, D. Qian, Y. Li, W. Zhang, Single-crystal α-MnO2 nanorods: synthesis and electrochemical properties, Nanotechnology 18 (2007) 115616.
[31] Z. Zhou, X. Liu, Z. Liao, H. Shao, Y. Hu, Y. Xu, M. Xu, A novel low temperature catalyst regenerated from deactivated SCR catalyst for Hg^0 oxidation, Chem. Eng. J. 304 (2016) 121–128.
[32] Z. Zhou, X. Liu, Z. Bo, H. Shao, Y. Xu, M. Xu, Elemental mercury oxidation over manganese-based perovskite-type catalyst at low temperature, Chem. Eng. J. 288 (2016) 701–710.
[33] D. Jampaiah, S.J. Ippolito, Y.M. Sabri, J. Tardio, P.R. Selvakannan, A. Nafady, B.M. Reddy, S.K. Bhargava, Ceria?zirconia modified MnOx catalysts for gaseous elemental mercury oxidation and adsorption, Catal. Sci. Technol. 6 (2016) 1792–1803.
[34] H.-Q. Wang, Z.-S. Li, Y.-G. Huang, Q.-Y. Li, X.-Y. Wang, A novel hybrid supercapacitor based on spherical activated carbon and spherical MnO 2 in a non-aqueous electrolyte, J. Mater. Chem. 20 (2010) 3883–3889.
[35] J. Luo, H. Zhu, H. Fan, J. Liang, H. Shi, G. Rao, J. Li, Z. Du, Z. Shen, Synthesis of single-crystal tetragonal α-MnO2 nanotubes, J. Phys. Chem. C 112 (2008) 12594–12598.